ACS Partner Journal

CHEMICAL & BIOMEDICAL IMAGING

Open Access

This article is licensed under CC-BY-NC-ND 4.0

pubs.acs.org/ChemBioImaging

Article

A Self-Immobilizing Photoacoustic Probe for Ratiometric In Vivo Imaging of Cu(II) in Tumors

Published as part of Chemical & Biomedical Imaging special issue "Bioimaging of Metals".

Qian Sun, Hang Liu, Ying Yang, Shankun Yao, Zhipeng Liu,* and Zijian Guo*

Cite This: *Chem. Biomed. Imaging* 2025, 3, 260−266

Read Online

ACCESS | Metrics & More | Article Recommendations | Supporting Information

ABSTRACT: Cu(II) ions play a critical role in tumor growth and metastasis, making in vivo high-resolution imaging of Cu(II) crucial for understanding its role in tumor pathophysiology. However, designing suitable molecular probes for this purpose remains challenging. Herein, we report the development of a photoacoustic probe for specific in vivo imaging of Cu(II) in tumors. This probe utilizes β-galactoside as a targeting group and incorporates a unique self-immobilization strategy. Upon β-galactosidase-mediated cleavage, the probe generates a reactive quinone methide intermediate that covalently binds to intracellular proteins, enabling selective tumor accumulation. The probe exhibits a ratiometric photoacoustic response to Cu(II) with high selectivity over that of other biological species. In vitro and in vivo studies demonstrated the efficacy of the probe for Cu(II) imaging in tumors. This research provides valuable insights into the role of Cu(II) in tumorigenesis and may facilitate the development of diagnostic and therapeutic approaches for cancer.

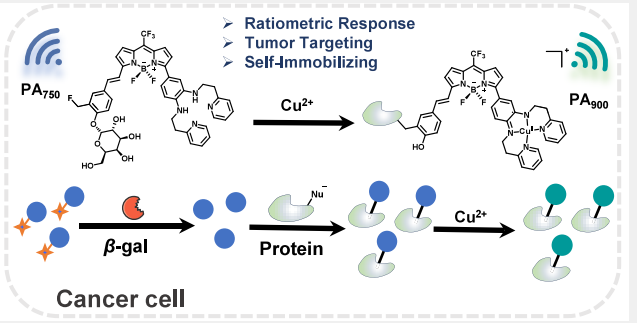

KEYWORDS: *molecule probes, photoacoustic imaging, copper homeostasis, tumor, in vivo imaging*

INTRODUCTION

Copper is an essential trace element that serves as a cofactor for numerous enzymes involved in vital physiological processes, including cellular respiration, neurotransmission, and antioxidant defense.[1−4] However, disruptions in copper homeostasis, leading to Cu(II) accumulation, are implicated in various diseases, including cancer.[5−9] Tumorigenesis is closely linked to copper homeostasis imbalance. Cu(II) ions play a critical role in regulating endothelial factors that drive tumor angiogenesis, a key process in tumor growth and metastasis. Research has demonstrated that the concentration of Cu(II) in malignant tumors is 46% higher than that in healthy tissues.[10−12] Therefore, accurate in vivo monitoring of Cu(II) in tumors using molecular probe technology is of great significance for understanding the role of Cu(II) in tumor development and progression.

Recent years have witnessed significant advancements in the development of Cu(II) fluorescent and magnetic resonance probes, enabling precise detection and imaging of Cu(II) in biological systems.[13−15] These probes have provided valuable insights into Cu(II)-related physiological and pathological functions. For instance, the Kim[16] and Lippard[17] groups developed "turn-off" luminescent probes that respond to Cu(II) via coordination mechanisms, facilitating dynamic imaging of Cu(II) in cells. The Chang group pioneered the use of an activity-based fluorescent probe, revealing the existence of intracellular Cu(II) pools under oxidative stress conditions.[18] The Sherry group designed and synthesized GdL1, an MRI probe for Cu(II) detection, by linking a biphenyl-2,2-dicarboxylic acid ligand with GdDO3A. This probe effectively detects excess Cu(II) in the mouse liver by forming a ternary complex with Cu(II) and HSA.[19] However, limitations such as fluorescence quenching by paramagnetic Cu(II), low resolution, and sensitivity issues inherent in fluorescence and MRI imaging hinder the application of these probes for high-resolution dynamic in situ imaging of Cu(II) within tumors.

Photoacoustic (PA) imaging, a noninvasive imaging modality, has garnered significant attention in the biomedical field due to its high sensitivity, resolution, and deep tissue penetration.[20,21] The development of diverse PA probes has expanded the capabilities of in vivo imaging, particularly for biologically relevant species.[22,23] PA imaging has shown great

Received: December 31, 2024
Revised: February 14, 2025
Accepted: February 17, 2025
Published: March 3, 2025

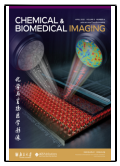

© 2025 The Authors. Co-published by Nanjing University and American Chemical Society

https://doi.org/10.1021/cbmi.4c00115
Chem. Biomed. Imaging 2025, 3, 260−266

promise for high-resolution in vivo imaging of Cu(II). The Chan group pioneered the development of a small-molecule Cu(II) PA probe (APC-2), demonstrating its potential for in vitro detection.[24] Subsequently, the Lin and Zhang groups reported PA probes LET-2 and RPS1, respectively, enabling Cu(II) imaging in plants and in the liver and brain of mice using two-dimensional PA imaging.[25,26] Our research group further advanced this field by designing a ratiometric PA probe (PACu3) and employing three-dimensional PA imaging technology to achieve microresolution imaging of Cu(II) in the brains of Parkinson's disease mice.[27] While these studies highlight the exceptional high-resolution imaging capabilities of PA probes for Cu(II) in vivo, the field remains in its early stages. Notably, the development and application of PA probes for the dynamic imaging of Cu(II) in living tumors have yet to be reported.

In this study, building upon our previous work, we developed photoacoustic probes, ***β*-gal-PA$_{Cu}$1** and ***β*-gal-PA$_{Cu}$2**, for highly selective Cu(II) imaging in tumors by exploiting the *β*-galactosidase activity. We incorporated *β*-galactoside and benzyl fluoride groups into the probe structure, endowing ***β*-gal-PA$_{Cu}$2** with excellent tumor-targeting capabilities. Furthermore, the probe can undergo self-immobilization to proteins via covalent cross-linking, significantly extending the retention time at the imaging site. This strategy facilitates high-resolution, precise in situ imaging and quantification of Cu(II) within tumor cells (Figure 1).

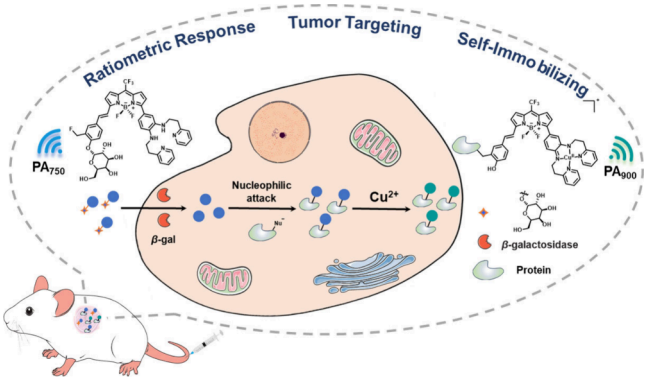

Figure 1. Chemical structure of ***β*-gal-PA$_{Cu}$2** and schematic illustration of ratiometric PA imaging in a tumor.

■ RESULTS AND DISCUSSIONS

Based on our previous work with CF_3−BODIPY-based PA probes (**PA$_{Cu}$1−3**),[27] which exhibited high selectivity for Cu(II) and excellent PA imaging capabilities, we sought to develop probes capable of high-resolution imaging of Cu(II) within tumors by incorporating tumor-targeting moieties. Since *β*-galactosidase is known to be upregulated in tumor initiation, progression, and metastasis, making it a valuable biomarker for tumor targeting,[28−30] we designed ***β*-gal-PA$_{Cu}$1** by incorporating a 2-(*β*-galactoside)-4-styrylphenyl group at the 3-position of CF_3−BODIPY. This modification was expected to enhance tumor accumulation of the probe through *β*-galactosidase-mediated recognition. To further improve probe retention within tumor tissue, we introduced a benzyl fluoride group at the *ortho*-position of the phenyl ring bearing the glycoside in a subsequent probe, ***β*-gal-PA$_{Cu}$2**. Upon *β*-galactosidase-mediated hydrolysis, the released quinone methide intermediate can undergo covalent cross-linking with nucleophilic groups on the enzyme,[31−34] facilitating targeted anchoring of the probe and minimizing signal loss due to probe efflux. To evaluate the impact of these modifications, we also synthesized **PA$_{Cu}$4** as a control probe. The synthesis routes for all probes are outlined in Schemes 1 and S1.

In MOPS buffer, ***β*-gal-PA$_{Cu}$1** and ***β*-gal-PA$_{Cu}$2** exhibited absorption maxima (λ_{abs}) at 748 and 750 nm, with molar absorption coefficients (ε) of 29600 and 26700 M^{-1} cm^{-1}, respectively (Figure 2a and Table S1). Furthermore, both of these probes displayed weak emission bands centered at 810 nm, with low fluorescence quantum yields (Φ_f) of 1.1% and 0.72%, respectively (Table S1). These findings suggest that a significant portion of the absorbed energy is converted into heat in the excited state, a characteristic that is favorable for efficient PA signal generation.[21]

To investigate the response behavior of ***β*-gal-PA$_{Cu}$1** and ***β*-gal-PA$_{Cu}$2** to Cu(II), titration experiments were performed by monitoring changes in the absorption spectra upon the addition of Cu(II) ions. Upon Cu(II) addition, the absorption intensity of ***β*-gal-PA$_{Cu}$1** at 748 nm decreased, while new absorption bands emerged at 635 and 787 nm. The presence of a clear isosbestic point in the spectra indicated the formation of a single Cu(II)−probe complex. The ratio of absorbance at 900 nm to that at 750 nm ($Abs_{900/750}$) increased gradually with increasing Cu(II) concentration, reaching saturation at a 1:1 Cu(II)/probe stoichiometry. ***β*-gal-PA$_{Cu}$2** exhibited a similar response behavior to Cu(II), suggesting that the introduction of the benzyl fluoride group did not interfere with the probe's Cu(II)-binding properties (Figure S1).

The bathochromic shift of the absorption band observed upon Cu(II) coordination is attributed to the formation of a free radical cation. This hypothesis is supported by electron paramagnetic resonance (EPR) spectroscopy, which revealed a strong radical signal (g = 2.16) in the Cu(II) complexes of ***β*-gal-PA$_{Cu}$1** and ***β*-gal-PA$_{Cu}$2**, while no radical signal was detected for the probes alone (Figures 2b and S2). We performed electrospray ionization mass spectrometry (ESI-MS) analysis to further characterize the formation of the Cu(II)−probe complex and its stoichiometric ratio. In the acetonitrile solution containing 1 equiv of Cu(II), the ESI-MS spectra of ***β*-gal-PA$_{Cu}$1** exhibited peaks at m/z 857.3243 and 917.2299, attributed to $[M + H]^+$ and $[M + Na]^+$ ions of the probe and its Cu(II) complex, respectively. Similar results were observed for ***β*-gal-PA$_{Cu}$2**, with peaks at m/z 889.3309 and 949.2375. These findings confirmed the formation of a 1:1 Cu(II)−probe complex (Figure S3). To determine the dissociation constants (K_d) of the Cu(II)−probe complexes, competition binding assays were performed using ethylene glycol-bis(2-aminoethyl ether)-*N*,*N*,*N*′,*N*′-tetraacetic acid (EGTA) as a Cu(II) chelator.[27] The measured K_d values were 514 pM for ***β*-gal-PA$_{Cu}$1** and 123 pM for ***β*-gal-PA$_{Cu}$2**, indicating the moderate affinity of these probes for Cu(II) and their potential for in vivo Cu(II) detection (Figures 2c and S4).

To assess the suitability of ***β*-gal-PA$_{Cu}$1** and ***β*-gal-PA$_{Cu}$2** for in vivo applications, we evaluated their selectivity and stability in complex biological environments. We investigated the probe response in the presence of various biologically relevant species, including reactive oxygen species (ROS), reactive sulfur species (RSS), and other ions. While Cu(II) addition resulted in a significant increase in the $Abs_{900/750}$ ratio, the presence of other species had negligible effects on the probe

https://doi.org/10.1021/cbmi.4c00115
Chem. Biomed. Imaging 2025, 3, 260−266

Scheme 1. Synthesis Routes of β-gal-PA$_{Cu}$1, β-gal-PA$_{Cu}$2, PA$_{Cu}$4, and PA$_{Cu}$5

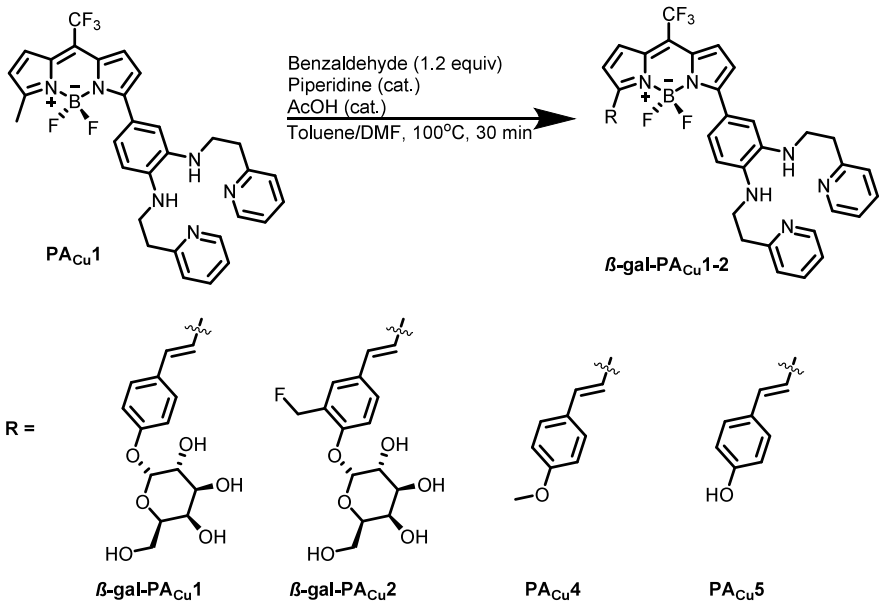

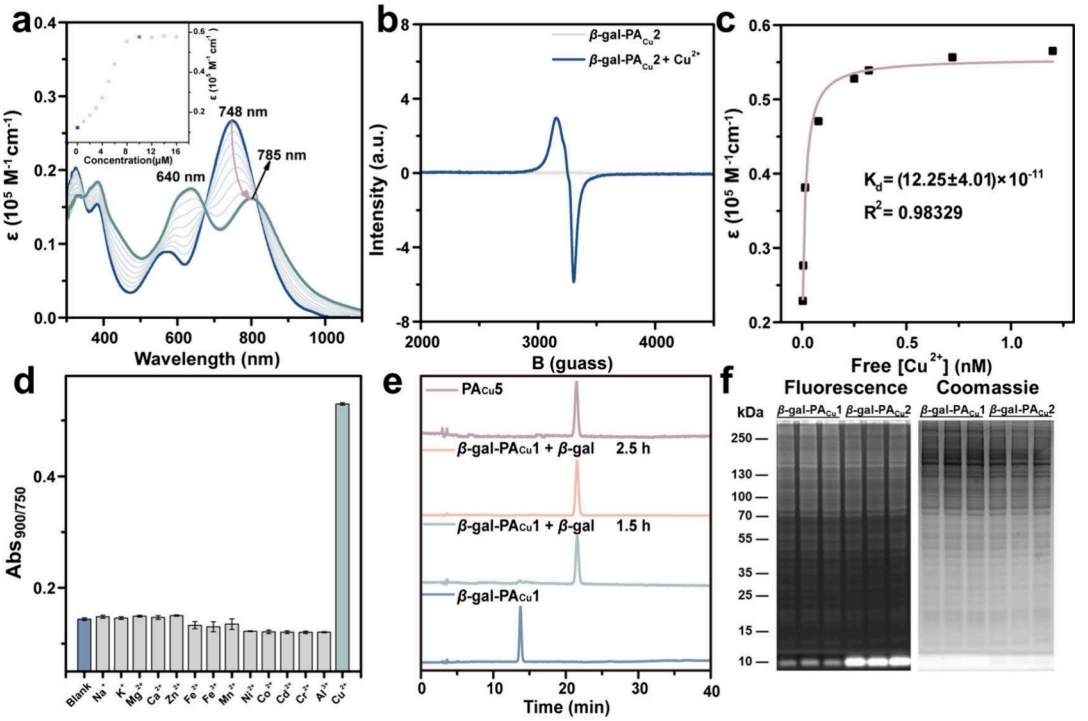

Figure 2. (a) Absorbance spectra of **β-gal-PA$_{Cu}$2** (10 μM) in MOPS buffer. (b) EPR spectra of **β-gal-PA$_{Cu}$2** (1 mM) and treatment with Cu(II) (1 mM) in the mixed solvent of MOPS buffer at room temperature. (c) Absorption ratio of **β-gal-PA$_{Cu}$2** as a function of the concentration of free Cu(II) in MOPS buffer. (d) Colorimetric ratio, Abs$_{900/750}$, of **β-gal-PA$_{Cu}$2** (10 μM) determined in the presence of Cu(II) and other analytes. Data are mean ± SEM, n = 3. (e) HPLC spectra of **β-gal-PA$_{Cu}$1** treated with β-galactosidase. (f) SDS-PAGE analyses of the lysate of 4T1 cells pretreated with **β-gal-PA$_{Cu}$1** and **β-gal-PA$_{Cu}$2**.

response. Notably, the probe exhibited minimal changes in absorption spectra in the presence of metal ions such as Zn(II), Ni(II), Mn(II), and Co(II). Although these divalent metal ions typically exhibit similar coordination behavior with Cu(II), the high affinity of the probe for Cu(II) compared to these divalent metal ions likely accounts for this selective response behavior.

Meanwhile, we also tested the anti-interference abilities of **β-gal-PA$_{Cu}$1** and **β-gal-PA$_{Cu}$2**. In the presence of biologically relevant species, **β-gal-PA$_{Cu}$1** and **β-gal-PA$_{Cu}$2** can remain undisturbed and still have a high response ability to Cu(II) (Figures 2d and S5). These results demonstrate the high selectivities of **β-gal-PA$_{Cu}$1** and **β-gal-PA$_{Cu}$2** for Cu(II) in a complex biological environment. Furthermore, we evaluated the pH stability of the probes (Figure S6). **β-gal-PA$_{Cu}$1** and **β-gal-PA$_{Cu}$2** exhibited excellent stability within the physiological pH range (4.0−10.0), with minimal impact on their Cu(II) response. Furthermore, we also investigated the stability of **β-**

https://doi.org/10.1021/cbmi.4c00115
Chem. Biomed. Imaging 2025, 3, 260−266

gal-PA$_{Cu}$1 and **β-gal-PA$_{Cu}$2** in MOPS and fetal bovine serum, respectively. Under 808 nm laser irradiation, the absorption spectra of **β-gal-PA$_{Cu}$1** and **β-gal-PA$_{Cu}$2** in these media did not change significantly (Figure S7), which indicates the good stability of **β-gal-PA$_{Cu}$1** and **β-gal-PA$_{Cu}$2**. These findings suggest that the probes are well-suited for in vivo PA imaging under physiological conditions.

We further performed HPLC-MS analysis to confirm the β-galactosidase targeting ability as well as β-galactosidase-mediated hydrolysis (Figures 2e and S8). **β-gal-PA$_{Cu}$1** exhibited a retention time of 13.7 min (m/z = 857.3280). Upon incubation with β-galactosidase, a new peak emerged at 21.5 min (m/z = 695.2752), indicating successful hydrolysis of the glycosidic bond. Complete hydrolysis of the probe was observed within 2.5 h.

To evaluate the binding ability of **β-gal-PA$_{Cu}$2**, we analyzed cell lysates from 4T1 cells treated with the probe by using SDS-PAGE (Figure 2f). Fluorescence was observed broadly across the protein molecular weight range following treatment with **β-gal-PA$_{Cu}$1** and **β-gal-PA$_{Cu}$2**, and a significant portion of the fluorescence was also observed at the electrophoresis front, likely due to interactions with small-molecule nucleophiles such as free amino acids, glutathione, and water. These findings suggest that activated **β-gal-PA$_{Cu}$2** undergoes covalent cross-linking with intracellular proteins and nucleophilic molecules such as amino acids, and the results indicate that **β-gal-PA$_{Cu}$2** exhibits better labeling efficiency. Furthermore, we investigated the effect of β-galactosidase-mediated hydrolysis on the UV−vis absorption spectra of the probe (Figure S9). No significant shifts in the absorption wavelength were observed following glycosidic bond cleavage.

To evaluate the PA imaging capabilities of **β-gal-PA$_{Cu}$1** and **β-gal-PA$_{Cu}$2**, we assessed their response to Cu(II) in MOPS buffer (Figures 3 and S10). The PA spectra closely mirrored the corresponding UV−vis absorption spectra, confirming the reliability of the UV−vis-based characterization. Upon the addition of Cu(II), the PA intensity of **β-gal-PA$_{Cu}$1** and **β-gal-PA$_{Cu}$2** decreased at 750 nm and increased at 900 nm. This resulted in a significant enhancement of the PA ratio ($PA_{900/750}$) by 1.32-fold. Importantly, a linear correlation was observed between the PA ratio and the Cu(II) concentration, and the PA limit of detection was calculated to be 660 nM. This demonstrated the potential of **β-gal-PA$_{Cu}$1** and **β-gal-PA$_{Cu}$2** for in vivo ratiometric PA imaging of Cu(II).

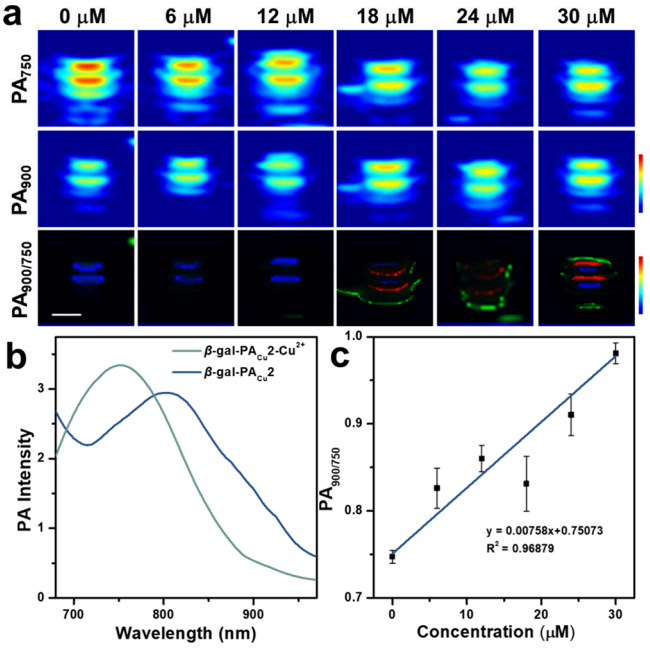

Figure 3. (a) Ratiometric PA imaging of **β-gal-PA$_{Cu}$2** (30 μM) in the presence of Cu^{2+} (0−30 μM). Scale bar: 0.2 mm. (b) PA spectra of **β-gal-PA$_{Cu}$2** with and without Cu^{2+} in PBS buffer. (c) $PA_{900/750}$ profile of **β-gal-PA$_{Cu}$2** determined at different Cu^{2+} concentrations and the linear fitting.

Next, we performed standard MTT assays to evaluate the biocompatibility of **β-gal-PA$_{Cu}$1** and **β-gal-PA$_{Cu}$2**. Incubation of HepG2 and HeLa cells with the probes for 24 h resulted in cell viabilities exceeding 90%, indicating low cytotoxicity. We also evaluated the toxicity of **β-gal-PA$_{Cu}$1** and **β-gal-PA$_{Cu}$2** in normal cells, and the probes had almost no toxicity to normal cells (Figure S11). To assess the in vivo PA imaging capabilities of the probes, we conducted 2D PA imaging to detect Cu(II) in 4T1 tumor-bearing mice. Four groups were included in the study: **PA$_{Cu}$4** (control), **β-gal-PA$_{Cu}$1**, **β-gal-PA$_{Cu}$2**, and ATTM (ammonium tetrathiomolybdate, a copper chelator)[35] (Figure 4a and S12). In the control group, no significant PA signal was detected at the tumor site. In the **β-gal-PA$_{Cu}$1** group, the PA signal initially increased but subsequently decreased after 3 h. In contrast, the **β-gal-PA$_{Cu}$2** group exhibited a sustained increase in PA signal following probe injection, with a gradual decrease observed only after 6 h. Ex vivo organ imaging further demonstrated the superior performance of **β-gal-PA$_{Cu}$2** (Figures S13−S15). The tumors in the **β-gal-PA$_{Cu}$2** group exhibited the strongest photoacoustic signals compared to the **PA$_{Cu}$4** and **β-gal-PA$_{Cu}$2** groups. In the ATTM group, weaker PA signal changes were detected at the tumor site. These findings strongly suggest that the introduction of the benzyl fluoride group significantly enhanced probe retention within the tumor, leading to improved PA imaging.

To obtain higher resolution and more comprehensive spatial distribution information, we employed 3D dual-channel PA tomography (Figure 4c and S16). In tumor-bearing mice injected with saline (control group), weak background PA signals were observed in both the 900 and 750 nm channels. Importantly, the negligible ratio signal ($PA_{900/750}$) in the ratio map demonstrated the effectiveness of self-calibration in minimizing background interference. To investigate the spatiotemporal distribution of Cu(II) within tumors, we monitored the accumulation of **β-gal-PA$_{Cu}$1** and **β-gal-PA$_{Cu}$2** following tail-vein injection. The $PA_{900/750}$ ratio gradually increased over time, indicating the formation of a Cu(II)−probe complex. This ratio reached a peak at approximately 6 h post-injection, suggesting optimal Cu(II) imaging at this time point. 3D imaging of tumors in mice injected with **β-gal-PA$_{Cu}$2** revealed a significantly higher $PA_{900/750}$ ratio compared to the **β-gal-PA$_{Cu}$1** and control groups. This resulted in a 5.4-fold increase in the ratio signal compared with the tumor + PBS group. The enhanced ratio signal provided a clearer tumor outline with a distinct spatial distribution pattern, confirming the superior tumor enrichment and targeting capabilities of the **β-gal-PA$_{Cu}$2**, and the signal of the probe retained in the tumor gradually disappeared after 12 h (Figure S17).

Tumors exhibit increased copper demand compared with normal tissues, particularly during rapid proliferation and angiogenesis, where Cu(II) plays a crucial role in cellular processes. To investigate the relationship between tumor

https://doi.org/10.1021/cbmi.4c00115
Chem. Biomed. Imaging 2025, 3, 260−266

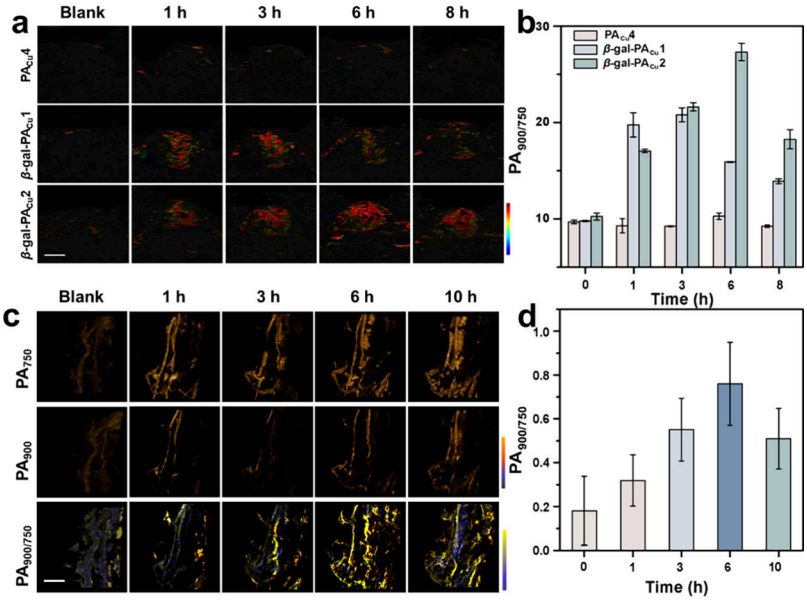

Figure 4. (a) 2D PA ratiometric images of 4T1 tumor mice injected with **PA$_{Cu}$4** (control), ***β*-gal-PA$_{Cu}$1**, and ***β*-gal-PA$_{Cu}$2**. Scale bar: 2 mm. (b) PA intensity ratios ($PA_{900/750}$) from (a). (c) 3D PA and ratiometric images of 4T1 tumor mice injected with ***β*-gal-PA$_{Cu}$2**. Scale bar: 5 mm (d) PA intensity ratios ($PA_{900/750}$) from (c).

growth and Cu(II) levels, we performed dynamic imaging of tumors at various growth stages (Figure 5a). Six hours post-injection of ***β*-gal-PA$_{Cu}$2**, PA images were acquired from tumors of different sizes. Consistent with previous findings, the PA signal distribution within the tumors was relatively uniform, facilitating accurate signal intensity quantification. Within the range of 50−200 mm^3, a clear correlation was observed between the tumor volume and the ratio of PA signals within the tumor. As tumor volume increased, the PA signal ratio also increased, suggesting a gradual increase in intratumoral Cu(II) concentration during tumor growth. In addition, the abdominal blood vessels with a diameter of 55 μm are clearly outlined in the 900 nm PA channel, achieving a signal-to-background ratio (SBR) of 11.56 db in the 3D visualization (Figure 5c). Therefore, the significant increase in the ratio and the favorable SBR contribute to clearer tumor imaging and more accurate distribution information on Cu(II) in the ratio images.

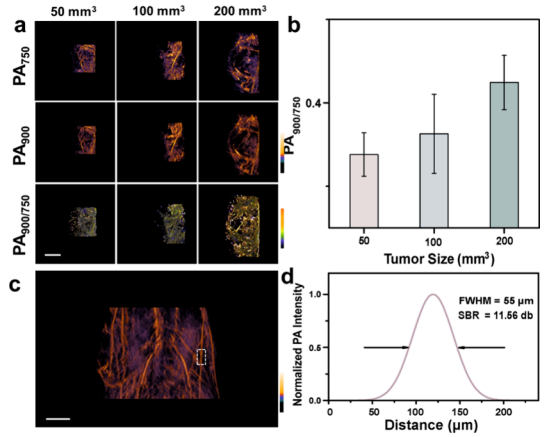

Figure 5. (a) Ratiometric 3D PA imaging ($PA_{900/750}$) of the 4T1 tumor mice injected with ***β*-gal-PA$_{Cu}$2** after 6 h. Scale bar: 5 mm. (b) The ratios of $PA_{900/750}$ from (a). (c) 3D PA imaging of the mouse post-***β*-gal-PA$_{Cu}$2** injection. Scale bar: 5 mm. (d) PA signal intensity and SBR value of the white solid line. fwhm: full width at half-maximum.

CONCLUSIONS

In summary, we have developed a PA probe, ***β*-gal-PA$_{Cu}$2**, for the in vivo imaging of Cu(II) in tumors. This probe exhibits excellent ratiometric PA response to Cu(II) with high selectivity in the presence of various biological molecules. By incorporating a *β*-galactoside moiety and a benzyl fluoride group, we endowed the probe with tumor-targeting capabilities and significantly prolonged its retention time within the tumor tissue. In vitro studies demonstrated the strong PA imaging potential and excellent biocompatibility. Utilizing a 4T1 tumor-bearing mouse model, we validated the probe's targeting ability, prolonged retention, and Cu(II) imaging capabilities in vivo. These findings suggest that ***β*-gal-PA$_{Cu}$2** is a promising tool for high-resolution imaging of Cu(II) in tumors. Compared to probes with solely targeting capabilities, the combination of tumor-targeting and subsequent self-immobilization not only extends probe retention time at the imaging site but also minimizes signal loss caused by probe efflux, thereby facilitating precise in vivo imaging of Cu(II) within tumor cells. This innovative approach may pave the way for the development of novel diagnostic and therapeutic strategies for cancer.

ASSOCIATED CONTENT

Data Availability Statement

The data supporting the findings of this study are available from the authors on reasonable request, see author contributions for specific data sets. Source data are provided with this paper.

Supporting Information

The Supporting Information is available free of charge at https://pubs.acs.org/doi/10.1021/cbmi.4c00115.

https://doi.org/10.1021/cbmi.4c00115
Chem. Biomed. Imaging 2025, 3, 260−266

Detailed synthetic procedures, chemical characterization, photophysical evaluation, biological evaluation, and in vivo imaging details (PDF)

AUTHOR INFORMATION

Corresponding Authors

Zijian Guo − *Chemistry and Biomedicine Innovation Center (ChemBIC), State Key Laboratory of Coordination Chemistry, School of Chemistry and Chemical Engineering, Nanjing University, Nanjing 210023, China;* orcid.org/0000-0003-4986-9308; Email: zguo@nju.edu.cn

Zhipeng Liu − *College of Materials Science and Engineering, College of Science, Co-Innovation Center of Efficient Processing and Utilization of Forest Resources, Nanjing Forestry University, Nanjing 210037, China;* orcid.org/0000-0002-5458-9362; Email: zpliu@njfu.edu.cn

Authors

Qian Sun − *Chemistry and Biomedicine Innovation Center (ChemBIC), State Key Laboratory of Coordination Chemistry, School of Chemistry and Chemical Engineering, Nanjing University, Nanjing 210023, China*

Hang Liu − *College of Materials Science and Engineering, College of Science, Co-Innovation Center of Efficient Processing and Utilization of Forest Resources, Nanjing Forestry University, Nanjing 210037, China*

Ying Yang − *Chemistry and Biomedicine Innovation Center (ChemBIC), State Key Laboratory of Coordination Chemistry, School of Chemistry and Chemical Engineering, Nanjing University, Nanjing 210023, China*

Shankun Yao − *Chemistry and Biomedicine Innovation Center (ChemBIC), State Key Laboratory of Coordination Chemistry, School of Chemistry and Chemical Engineering, Nanjing University, Nanjing 210023, China*

Complete contact information is available at: https://pubs.acs.org/10.1021/cbmi.4c00115

Notes

The authors declare no competing financial interest.

ACKNOWLEDGMENTS

National Natural Science Foundation of China (22377057, 22371124, 22293050, and 22293051), the Excellent Research Program of Nanjing University (ZYJH004), and the Natural Science Foundation of Jiangsu Province (BK20231298, BK20221333, and BK20232020).

REFERENCES

(1) Tsvetkov, P.; Coy, S.; Petrova, B.; Dreishpoon, M.; Verma, A.; Abdusamad, M.; Rossen, J.; Joesch-Cohen, L.; Humeidi, R.; Spangler, R. D.; Eaton, J. K.; Frenkel, E.; Kocak, M.; Corsello, S. M.; Lutsenko, S.; Kanarek, N.; Santagata, S.; Golub, T. R. Copper induces cell death by targeting lipoylated TCA cycle proteins. *Science* **2022**, *375* (6586), 1254−1261.

(2) Xiao, T.; Ackerman, C. M.; Carroll, E. C.; Jia, S.; Hoagland, A.; Chan, J.; Thai, B.; Liu, C. S.; Isacoff, E. Y.; Chang, C. J. Copper regulates rest-activity cycles through the locus coeruleus-norepinephrine system. *Nat. Chem. Biol.* **2018**, *14* (7), 655−663.

(3) Lippard, S. J.; Berg, J. M. *Principles of Bioinorganic Chemistry*; University Science Books: Mill Valley, CA, 1994.

(4) Wang, C.; Yuan, F.; Yan, Z.; Zhang, T.; Fu, C.; Li, Y.; Dai, G.; Kim, H. S.; Xia, S.; Yu, L.; Debnath, S.; Ren, W. X.; Shu, J.; Qiu, M.; Kim, J. S. High Entropy 2D Layered Double Hydroxide Nanosheet Toward Cascaded Nanozyme-Initiated Chemodynamic and Immune Synergistic Therapy. *J. Am. Chem. Soc.* **2025**, *147* (1), 136−148.

(5) Ge, E. J.; Bush, A. I.; Casini, A.; Cobine, P. A.; Cross, J. R.; DeNicola, G. M.; Dou, Q. P.; Franz, K. J.; Gohil, V. M.; Gupta, S.; Kaler, S. G.; Lutsenko, S.; Mittal, V.; Petris, M. J.; Polishchuk, R.; Ralle, M.; Schilsky, M. L.; Tonks, N. K.; Vahdat, L. T.; Van Aelst, L.; Xi, D.; Yuan, P.; Brady, D. C.; Chang, C. J. Connecting copper and cancer: from transition metal signalling to metalloplasia. *Nat. Rev. Cancer* **2022**, *22* (2), 102−113.

(6) Solier, S.; Müller, S.; Cañeque, T.; Versini, A.; Mansart, A.; Sindikubwabo, F.; Baron, L.; Emam, L.; Gestraud, P.; Pantoş, G. D.; Gandon, V.; Gaillet, C.; Wu, T.-D.; Dingli, F.; Loew, D.; Baulande, S.; Durand, S.; Sencio, V.; Robil, C.; Trottein, F.; Péricat, D.; Näser, E.; Cougoule, C.; Meunier, E.; Bègue, A.-L.; Salmon, H.; Manel, N.; Puisieux, A.; Watson, S.; Dawson, M. A.; Servant, N.; Kroemer, G.; Annane, D.; Rodriguez, R. A druggable copper-signalling pathway that drives inflammation. *Nature* **2023**, *617* (7960), 386−394.

(7) Davies, K. M.; Bohic, S.; Carmona, A.; Ortega, R.; Cottam, V.; Hare, D. J.; Finberg, J. P. M.; Reyes, S.; Halliday, G. M.; Mercer, J. F. B.; Double, K. L. Copper pathology in vulnerable brain regions in Parkinson's disease. *Neurobiol. Aging* **2014**, *35* (4), 858−866.

(8) Desai, V.; Kaler, S. G. Role of copper in human neurological disorders. *Am. J. Clin. Nutr.* **2008**, *88* (3), 855S−858S.

(9) Gaggelli, E.; Kozlowski, H.; Valensin, D.; Valensin, G. Copper homeostasis and neurodegenerative disorders (Alzheimer's, prion, and Parkinson's diseases and amyotrophic lateral sclerosis). *Chem. Rev.* **2006**, *106* (6), 1995−2044.

(10) Margalioth, E. J.; Schenker, J. G.; Chevion, M. Copper and Zinc levels in normal and malignant tissues. *Cancer* **1983**, *52* (5), 868−872.

(11) Florianczyk, B. Copper and metallothioneins in cancer cells. *Ann. Univ. Mariae Curie Sklodowska Med.* **2003**, *58* (2), 390−393.

(12) Gupte, A.; Mumper, R. J. Elevated copper and oxidative stress in cancer cells as a target for cancer treatment. *Cancer Treat. Rev.* **2009**, *35* (1), 32−46.

(13) Yin, C.; Li, J.; Huo, F. Cu^{2+} Biological Imaging Probes Based on Different Sensing Mechanisms. *Curr. Med. Chem.* **2019**, *26* (21), 3958−4002.

(14) Chopra, T.; Sasan, S.; Devi, L.; Parkesh, R.; Kapoor, K. K. A comprehensive review on recent advances in copper sensors. *Coord. Chem. Rev.* **2022**, *470*, 214704.

(15) Pierre, V. C.; Harris, S. M.; Pailloux, S. L. Comparing Strategies in the Design of Responsive Contrast Agents for Magnetic Resonance Imaging: A Case Study with Copper and Zinc. *Acc. Chem. Res.* **2018**, *51* (2), 342−351.

(16) Jung, H. S.; Kwon, P. S.; Lee, J. W.; Kim, J. I.; Hong, C. S.; Kim, J. W.; Yan, S.; Lee, J. Y.; Lee, J. H.; Joo, T.; Kim, J. S. Coumarin-derived Cu(2+)-selective fluorescence sensor: synthesis, mechanisms, and applications in living cells. *J. Am. Chem. Soc.* **2009**, *131* (5), 2008−2012.

(17) You, Y.; Han, Y.; Lee, Y. M.; Park, S. Y.; Nam, W.; Lippard, S. J. Phosphorescent sensor for robust quantification of copper(II) ion. *J. Am. Chem. Soc.* **2011**, *133* (30), 11488−11491.

(18) Pezacki, A. T.; Matier, C. D.; Gu, X.; Kummelstedt, E.; Bond, S. E.; Torrente, L.; Jordan-Sciutto, K. L.; DeNicola, G. M.; Su, T. A.; Brady, D. C.; Chang, C. J. Oxidation state-specific fluorescent copper sensors reveal oncogene-driven redox changes that regulate labile copper(II) pools. *Proc. Natl. Acad. Sci. U.S.A.* **2022**, *119* (43), No. e2202736119.

(19) Paranawithana, N. N.; Martins, A. F.; Clavijo Jordan, V.; Zhao, P.; Chirayil, S.; Meloni, G.; Sherry, A. D. A Responsive Magnetic Resonance Imaging Contrast Agent for Detection of Excess Copper(II) in the Liver In Vivo. *J. Am. Chem. Soc.* **2019**, *141* (28), 11009−11018.

(20) Wang, L. V.; Hu, S. Photoacoustic tomography: in vivo imaging from organelles to organs. *Science* **2012**, *335* (6075), 1458−1462.

(21) Kim, C.; Favazza, C.; Wang, L. V. In vivo photoacoustic tomography of chemicals: high-resolution functional and molecular optical imaging at new depths. *Chem. Rev.* **2010**, *110* (5), 2756−2782.

(22) Liu, Y.; Teng, L.; Yin, B.; Meng, H.; Yin, X.; Huan, S.; Song, G.; Zhang, X. B. Chemical Design of Activatable Photoacoustic Probes for Precise Biomedical Applications. *Chem. Rev.* **2022**, *122* (6), 6850−6918.
(23) Knox, H. J.; Chan, J. Acoustogenic Probes: A New Frontier in Photoacoustic Imaging. *Acc. Chem. Res.* **2018**, *51* (11), 2897−2905.
(24) Li, H.; Zhang, P.; Smaga, L. P.; Hoffman, R. A.; Chan, J. Photoacoustic Probes for Ratiometric Imaging of Copper(II). *J. Am. Chem. Soc.* **2015**, *137* (50), 15628−15631.
(25) Zeng, L.; Ma, G.; Xu, H.; Mu, J.; Li, F.; Gao, X.; Deng, Z.; Qu, J.; Huang, P.; Lin, J. In Vivo Chemoselective Photoacoustic Imaging of Copper(II) in Plant and Animal Subjects. *Small* **2019**, *15* (6), No. 1803866.
(26) Wang, S.; Sheng, Z.; Yang, Z.; Hu, D.; Long, X.; Feng, G.; Liu, Y.; Yuan, Z.; Zhang, J.; Zheng, H.; Zhang, X. Activatable Small-Molecule Photoacoustic Probes that Cross the Blood-Brain Barrier for Visualization of Copper(II) in Mice with Alzheimer's Disease. *Angew. Chem., Int. Ed.* **2019**, *58* (36), 12415−12419.
(27) Jiang, Z.; Zhang, C.; Wang, X.; Ling, Z.; Chen, Y.; Guo, Z.; Liu, Z. A Small-Molecule Ratiometric Photoacoustic Probe for the High-Spatiotemporal-Resolution Imaging of Copper(II) Dynamics in the Mouse Brain. *Angew. Chem., Int. Ed.* **2024**, *63*, No. e202318340.
(28) Bosmann, H. B.; Hall, T. C. Enzyme Activity in Invasive Tumors of Human Breast and Colon. *Proc. Natl. Acad. Sci. U. S. A.* **1974**, *71* (5), 1833−1837.
(29) Olszewska, E.; Borzym-Kluczyk, M.; Rzewnicki, I.; Wojtowicz, J.; Rogowski, M.; Pietruski, J. K.; Czajkowska, A.; Sieskiewicz, A. Possible role of α-mannosidase and β-galactosidase in larynx cancer. *Wspolczesna Onkol.* **2012**, *16* (2), 154−158.
(30) Wielgat, P.; Walczuk, U.; Szajda, S.; Bień, M.; Zimnoch, L.; Mariak, Z.; Zwierz, K. Activity of lysosomal exoglycosidases in human gliomas. *J. Neuro-Oncol.* **2006**, *80* (3), 243−249.
(31) Chiba, M.; Kamiya, M.; Tsuda-Sakurai, K.; Fujisawa, Y.; Kosakamoto, H.; Kojima, R.; Miura, M.; Urano, Y. Activatable Photosensitizer for Targeted Ablation of lacZ-Positive Cells with Single-Cell Resolution. *ACS Cent. Sci.* **2019**, *5* (10), 1676−1681.
(32) Doura, T.; Kamiya, M.; Obata, F.; Yamaguchi, Y.; Hiyama, T. Y.; Matsuda, T.; Fukamizu, A.; Noda, M.; Miura, M.; Urano, Y. Detection of LacZ-Positive Cells in Living Tissue with Single-Cell Resolution. *Angew. Chem., Int. Ed.* **2016**, *55* (33), 9620−9624.
(33) Zhu, Q.; Girish, A.; Chattopadhaya, S.; Yao, S. Q. Developing novel activity-based fluorescent probes that target different classes of proteases. *Chem. Commun.* **2004**, No. 13, 1512−1513.
(34) Zhang, Y.; Liu, S.; Guo, F.; Qin, S.; Zhou, N.; Liu, Z.; Fan, X.; Chen, P. R. Bioorthogonal Quinone Methide Decaging Enables Live-Cell Quantification of Tumor-Specific Immune Interactions. *J. Am. Chem. Soc.* **2024**, *146* (22), 15186−15197.
(35) Maiti, B. K.; Moura, J. J. G. Diverse biological roles of the tetrathiomolybdate anion. *Coord. Chem. Rev.* **2021**, *429*, 213635.

https://doi.org/10.1021/cbmi.4c00115
Chem. Biomed. Imaging 2025, 3, 260−266